

Noise Radiated by an Open Cavity at Low Mach Number

R. Martin^{*,**}, M. Soria^{*}, O. Lehmkuhl^{***}, A. Gorobets^{****}, J. Cante^{*} and P. Vidal^{**}
Corresponding author: manel.soria@upc.edu

^{*} Universitat Politècnica de Catalunya, Spain.

^{**} SEAT, Spain.

^{***} Barcelona Supercomputing Center, Spain.

^{****} Keldysh Institute of Applied Mathematics of RAS, Russia.

Abstract: The present work focuses on the study of noise generation and radiation of unsteady laminar flow over an open three dimensional cavity at low Mach number, that is of interest to understand noise generation mechanisms in wall-bounded separated flows. The length to depth ratio of the cavity is $L/D=4$. While this configuration has been extensively studied, most of the works assume the flow to be two-dimensional. However, as it will be shown, previous studies confirm that for Reynolds numbers above ≈ 1200 , the flow shows a three dimensional behaviour. This results in significantly different sound sources. This paper presents results of sound calculation radiated by a three-dimensional infinite open cavity at Reynolds number based on the cavity depth of $Re = 1500$ and Mach number of $M = 0.15$. To do so, two approaches have been used: Curle integral, evaluated as a post-process of an incompressible solution and compressible direct simulation. The results are also compared with the resulting Curle post-process of a two-dimensional incompressible simulation assumed to be constant along the spanwise direction.

Keywords: Computational Aeroacoustics, Low Mach Number, Curle Method, Direct Simulation.

1 Introduction

Aeroacoustics is a topic of research with increasing relevance due to its technological and societal implications. It is of particular interest to the automotive industry the study of flow past vehicles and the noise induced by it [1-3]. To mention a few works, [1] studied the noise generated by the air flow around the A-pillar and the side mirror of a generic vehicle model while [2,3] investigated the half cylinder and the hemisphere, respectively, as a simplification of side mirrors. Uncovered cavities, the object of the present work, are also usual parts of vehicle designs and their acoustic performance is a key issue of comfort for passengers or outside listeners.

As it is well known and extensively documented in [4], computational aeroacoustics cases can be addressed from two general approaches: Direct Simulation (DS) and hybrid approaches. Direct simulation is based on the resolution of the compressible Navier-Stokes equations without using any modelling of the sound. This method is the most direct way to compute sound generation since the governing equations completely describe the physics of the problem. However, solving the full set of equations implies extreme computational costs, out of the scope for the majority of industrial applications. Some of the reasons that make of compressible simulations a difficult approach to be used are: i) the disparity in length and time scales between fluid dynamics and acoustics, ii) in order to correctly capture the wave propagation, at least a few nodes per wavelength are needed, so the mesh cannot be coarsened much resulting in meshes with high number of elements and iii) boundary conditions are critical due to the reflection of acoustic waves into the domain.

On the other hand, for industrial problems, hybrid approaches seem to be more promising to predict aeroacoustic noise. These consist on two different numerical solvers: a purely CFD tool as the source generator and an acoustic solver as the transport method. Acoustic propagation methods can be divided into: Partial Differential Equations (PDE) methods and integral methods. PDE methods, such as Linear

Euler Equations (LEE), [5,6], or APE, [7], solve a system of PDEs describing the acoustic wave propagation in the entire field. The Computational Fluid Dynamics (CFD) solution is used as the exciting source for the system of PDEs solved in the aeroacoustic simulation. Owing to the change in discretization and resolution, proper coupling between the Navier Stokes solver and the wave solver is a nontrivial task. Integral approaches are mainly based on the work of James Lighthill, [8]. These methods integrate the relevant aerodynamic variables for acoustics propagation over a certain region to obtain the sound pressure at a certain observer in a certain time. Often integral approaches are referred as 'analogies' since they intend to find a wave equation propagating in a medium at rest excited by sources generated from the region where the fluid is in motion. From the computational point of view, integral methods are simpler and allow to have an explicit solution for the acoustic pressure which has to be numerically evaluated from the source terms obtained in the Navier Stokes solver. Two of the most widely used integral methods are the extension of Lighthill's theory for the interaction of the fluid with a surface, known as Curle's solution [9], and for the interaction of the fluid with a surface in motion, Ffwoes-Williams and Hawkings (FW-H) solution [10]. J.E. Ffwoes Williams and D.L. Hawkings generalised the Lighthill's solution for equivalent sources arising from moving surfaces immersed in the flow, while Curle rewrote the solution for the Lighthill's system when the boundary of the domain includes a solid surface at rest.

A broad body of literature on cavity noise computation has been developed over the last decade. The first computations of acoustic radiation from a cavity have been carried out by J.Hardin and D.Pope in [11]. The authors investigated the sound generated by an open cavity with aspect ratio $L/D = 4$ at Reynolds number based on the cavity length $Re_L = 5000$ and Mach number $M = 0.1$ using a two-part calculation where the viscous flow was first handled by calculating the time-dependent incompressible flow, and then the acoustic radiation was obtained from inviscid equations describing the differences from the incompressible flow. Later, Colonius et al. [12] used DS for aspect ratios ranging from 1 to 5 at a Reynolds number based on cavity depth $Re_D = 5000$ to directly compute the acoustic pressure. Gloerfelt et al. [13] studied the acoustic field of an open cavity with aspect ratio $L/D = 2$ at high Reynolds number, $Re_D = 4.1 \cdot 10^4$, and high subsonic speed, $M = 0.7$, using three different formulations: DS, Fwoes-Williams Hawkings and Wave Extrapolation Methods (WEM). More recently, L.Davidson et al. investigated in [14–16] the open cavity with aspect ratio $L/D = 4$ for Reynolds number $Re_D = 1500$ and Mach number $M = 0.15$ using first a modified version of Curle's integral for later comparison with DS.

Nevertheless, the aforementioned works have only considered the two-dimensional behaviour of flow past cavities assuming homogeneity in the spanwise direction. However, for $Re_D = 1500$, cavities of aspect ratio $L/D = 4$ have passed the transitional point and are reported to generate three dimensional vortical structures [17], resulting in very different flow fields. Likewise, experimental results are in agreement with these characterisation [18]. On the other hand, some researchers have investigated numerically the noise generated by an open three dimensional cavity with fixed width. Using the FW-H formulation, the acoustic field of a cavity with parameters $L/D = 5$ and $W/D = 1$ has been addressed by H.Lai and K.Luo [19] at Reynolds number $Re = 1.36 \cdot 10^6$ and Mach number $M = 0.85$.

The aim of this paper is to understand the acoustic behaviour of a three-dimensional open cavity and highlight the differences in results when a two-dimensional flow is considered as source term for the Curle integral. The case under study is an open cavity with aspect ratio $L/D = 4$, unconfined in the spanwise direction for $Re_D = 1500$ and $M = 0.15$. A modified version of the integral formulation derived by Curle in [9] will be used to calculate the acoustic field. The results will be compared with the acoustics generated by the same configuration considering a two-dimensional source flow. In order to gain a better insight of Curle's formulation, the acoustic field is also compared with the one obtained without any modelling of the sound, DS.

This paper is organised as follows. Section 2 gives a description of the hybrid method developed by Curle for predicting the acoustic response due to flow past a solid body. In section 3 the case under study is presented followed by the description of the numerical methods used to address the case in section 4. Section 5 shows the results obtained for the flow and acoustic fields comparing both between the two-dimensional (2D) with the three-dimensional (3D) approach and the Curle analogy with the compressible DS.

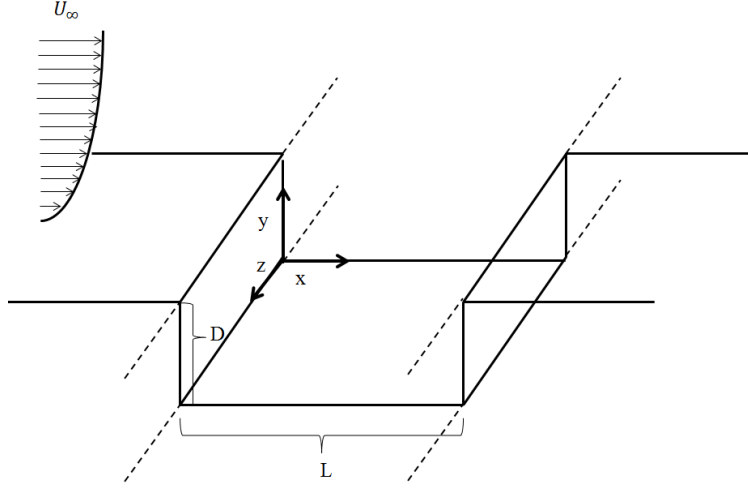


Figure 1: Geometry of the cavity.

2 Computational Aeroacoustics Method

In [8] Lighthill considered the compressible continuity and momentum equations under no external forces:

$$\frac{\partial \rho}{\partial t} + \frac{\partial}{\partial x_i} \rho u_i = 0 \quad (1)$$

$$\frac{\partial}{\partial t} \rho u_i + \frac{\partial}{\partial x_j} (\rho u_i u_j + p_{ij} - \tau_{ij}) = 0 \quad (2)$$

where x_i are the spatial coordinates (or x , y and z), u_i are the velocity components (or u , v and w), p is the pressure, ρ is the density and τ_{ij} is the viscous stress tensor:

$$\tau_{ij} = \mu \left(\frac{\partial u_i}{\partial x_j} + \frac{\partial u_j}{\partial x_i} - \frac{2}{3} \frac{\partial u_k}{\partial x_k} \delta_{ij} \right) \quad (3)$$

A simple mathematical manipulation of the previous equations lead to the inhomogeneous wave equation

$$\frac{\partial^2 \rho}{\partial t^2} - a_0^2 \nabla^2 \rho = \frac{\partial^2}{\partial x_i \partial x_j} (\rho u_i u_j + p_{ij} - a_0^2 \rho \delta_{ij} - \tau_{ij}) \quad (4)$$

where $T_{ij} = \rho u_i u_j + p_{ij} - a_0^2 \rho \delta_{ij} - \tau_{ij}$ is known as the Lighthill's stress tensor. Lighthill showed that for isentropic flows at low Mach numbers where viscous effects could be neglected, it is sufficient to assume $T_{ij} = \rho u_i u_j + p_{ij} - a_0^2 \rho \delta_{ij} - \tau_{ij} \approx \rho u_i u_j$.

The Curle's solution for the Lighthill's formulation is given by Eq.5:

$$\rho(\mathbf{x}, t) - \rho_0 = \frac{1}{4\pi a_0^2} \frac{\partial^2}{\partial x_i \partial x_j} \int_V \frac{[T_{ij}]}{r} dV + \frac{1}{4\pi a_0^2} \frac{\partial}{\partial x_i} \int_S \frac{n_j}{r} [p_{ij} - \tau_{ij}] dS \quad (5)$$

where the expression in brackets stands for the evaluation of the expression at the retarded time $\tau = t - r/a_0$, \mathbf{n} is the surface normal vector pointing to the surface and r is the distance between the observer position and the source point.

Curle's integral accounts for two type of sources: a quadrupole source arising from the volume integral (first term) and a dipole source arising from the surface integral (second term). Quadrupoles sources are less efficient producing acoustic waves than monopoles or dipoles sources, specially for low Mach numbers. In [9], it was shown that for low Mach number flows the relation between the acoustic power generated by

quadrupoles and dipoles is related by the Mach number:

$$\frac{P_{quad}}{P_{dip}} \approx M^2 \quad (6)$$

This justifies that the authors of [16, 20], working at $M = 0.15$ and $M = 0.2$ respectively, considered volumetric sources negligible. In [21], it was numerically confirmed that the contribution of the source terms inside the volume integral for the cavity case at $M = 0.15$ were several orders of magnitude smaller than the source terms inside the surface integral.

In order to implement Eq.5 the derivatives need to be taken inside the integral and spatial derivatives need to be transformed into time derivatives. This procedure was first done by Myers and Farassat in [22] to modify the solution of Kirchhoff's formula, primarily used in the theory of diffraction of light and in other electromagnetic problems, [23].

$$p(\mathbf{x}, t) - p_0 = \frac{1}{4\pi} \int_V \left(\frac{l_i l_j}{a_0^2 r} [\ddot{T}_{ij}] + \frac{3l_i l_j - \delta_{ij}}{a_0 r^2} [\dot{T}_{ij}] + \frac{3l_i l_j - \delta_{ij}}{r^3} [T_{ij}] \right) dV + \frac{1}{4\pi} \int_S -l_i n_j \left(\frac{1}{r a_0} [\dot{p}_{ij}] + \frac{1}{r^2} [p_{ij}] \right) dS \quad (7)$$

where the viscous term have been omitted and assuming isentropy, ρ has been transformed to p . The vector \mathbf{l} is the unitary vector pointing from the source point to the observational point:

$$l_i = \frac{x_i - y_i}{r} \quad (8)$$

A very important advantage of using Curle's formulation when it is reduced to a surface integral is that it provides direct information about the contribution of each point of the surface to the total acoustic power. This is of very much use in the industry since it highlights the most optimizable parts of the surface. In the recent years, techniques based on beamforming analysis combined with an acoustic technique are used for the localisation of sound sources [24]. However, the most important benefit of Curle's formulation is the allowance of an incompressible simulation as a source for the transient flow variables over the solid body when the Mach number is low and when the source region is considered compact. Moreover, the low Mach number allows to neglect the volume integral which would be computationally expensive and only take into account pressure effects over the surface.

Special attention needs to be taken into the compactness of the body when using Curle's integral, which, as previously stated, for low Mach numbers considers the solid boundaries as a distribution of dipole sources. This replacement is not possible for any configuration and it is recommended to ensure that the source region is acoustically compact before proceeding to the Curle post-processing. Mathematically, the acoustic compactness is defined in terms of the Helmholtz number [25]:

$$He = \frac{2\pi f D}{a_0} < 1 \quad (9)$$

The case of study presented in the following section accomplishes that the relative position between the source and the observers is constant, $\mathbf{v} = 0$, and that the Mach number is considered low, so the use of the Curle approach using an incompressible simulation as source terms is justified for those frequencies assuring compactness. Its validity will be contrasted with the results for the acoustic pressure obtained with a compressible simulation.

3 Problem Statement

The Curle analogy is applied to study the aeroacoustic radiation of an open cavity in presence of an upstream laminar flow, using three different models: two-dimensional incompressible, three-dimensional incompressible and three-dimensional compressible. The Reynolds number based on the cavity depth is defined as $Re_D = \frac{\rho_\infty U_\infty D}{\mu}$, where U_∞ is the freestream velocity, ρ_∞ is the freestream density and μ the dynamic viscosity of the

fluid. In the present case, $U_\infty = 1.0$, $\rho = 1.0$, $D = 1$ and $Re_D = 1500$. The Mach number is $M = \frac{U_\infty}{a_0} = 0.15$, where a_0 is the sound speed in the fluid.

The geometrical parameters of the cavity are $L/D = 4$, where L and D are the length and depth of the cavity respectively (see Fig.1). These parameters are indefinitely extended along the z direction (henceforth unconfined configuration). The origin of the domain is located at the leading edge of the cavity. The inlet domain is bounded at $x = -5D$ and the outlet at $x = 25D$ for both approaches, compressible and incompressible. However, previous test cases have shown that numerical calculation performs better when the upper part of the domain is located at $y = 10D$ for the compressible simulation and at $y = 12D$ for the incompressible.

Previous works on open cavity flows show that the thickness of the boundary layer arriving at the leading edge of the cavity can substantially change the behaviour of the flow around the cavity [12, 26]. M.Gharib and A.Roshko experimentally proved that the modes of oscillation of the cavity could be changed between non-oscillatory, shear layer mode and wake mode depending on the value of θ/L , where θ is the momentum thickness at the leading edge of the cavity. In order to make the results from different approaches comparable, it has been imposed that the boundary layer arriving at the leading edge of the cavity has the profile of the Blasius solution for a flat plate developed during 10 length units, i.e, having a $\delta_{0.99} \approx 0.4D$. For this reason the imposed inlet boundary condition is the velocity field corresponding to the Blasius solution developed during 5 length units. The tabulated Blasius solution has been fitted to the following expression:

$$\frac{u}{U_\infty}(y/D) = 1.0 - e^{-22.837905(y/D)^{1.4288577}} \quad (10)$$

Figure 2 shows the Blasius profile compared with expression 10.

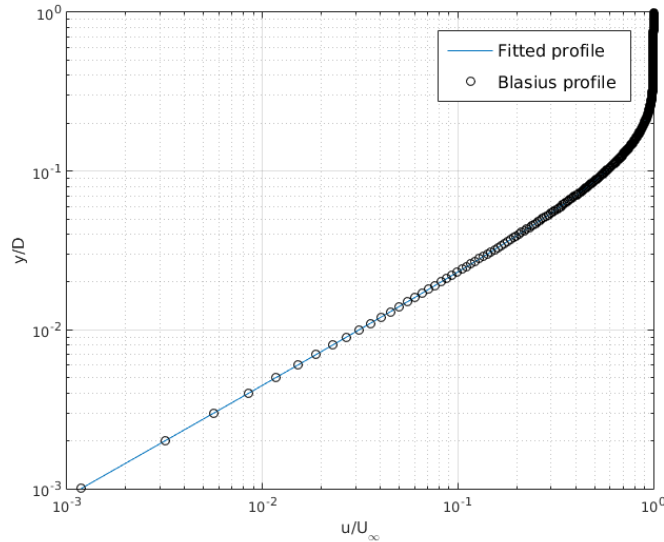


Figure 2: Tabulated Blasius solution and adjusted profile.

Considering that the cavity is infinite in the spanwise direction, periodic boundary conditions have been imposed at the front and back boundary walls. The extension of the cavity in the z direction has to be long enough to ensure the correct definition of the vortex structures. Figures 3 and 4 display the correlation coefficient when the width of the domain is 4 for two different (x, y) positions defined as:

$$R_{ii} = \frac{\langle u'_i(x_i, t)u'_i(x_i + \delta, t) \rangle}{\langle u'_i u'_i \rangle} \quad (11)$$

where $\langle * \rangle$ denotes the time average and $u'_i = u_i - \bar{u}_i$ the velocity fluctuation. As seen in Figures 3 and 4, the coefficient tends to zero as it approaches the half-size of the domain for the three components of the

velocity, a characteristic behaviour of turbulent flows. These results confirm that a width of 4 is enough to have statistically uncorrelated flow variables in the spanwise direction.

No slip boundary conditions are used in solid boundaries. Flow variables at the outflow boundary are specified by zero normal derivatives. However, in order to avoid reflections of pressure waves into the domain when solving the set of compressible Navier-Stokes equations, a buffer zone is imposed for the last 6 length units of the domain. The same procedure is used for the last 10 mesh elements of the domain (2 length units approximately at plane $y = 0$) when working with the two-dimensional incompressible simulation to completely damp the vortical structures. These vortices do not vanish with distance due to the non-existence of vortex stretching in two-dimensional.

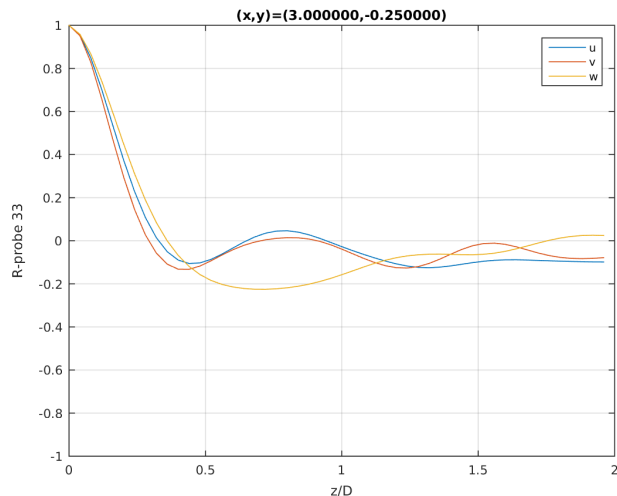


Figure 3: Correlation of velocity fluctuations along the z axis at $(x, y) = (3, -0.25)$.

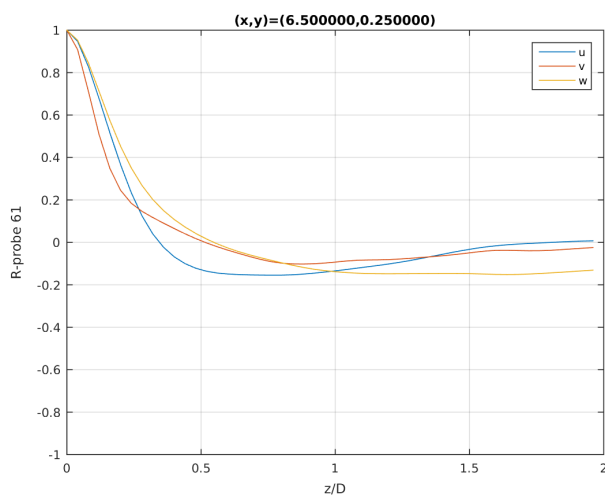


Figure 4: Correlation of velocity fluctuations along the z axis at $(x, y) = (6.5, 0.25)$.

4 Computational Methods

Two different CFD codes have been used to simulate the flow over the 3D cavity. To solve the governing equations based on the incompressible Navier Stokes equations it has been used Alya, a CFD code developed by Barcelona Supercomputing Center, [27]. For the compressible Navier Stokes equations it has been used NOISEtte, a CFD code developed by the Keldysh Institute of the Russian Association of Mathematics. Both set of equations have been solved without any turbulence model.

4.1 Numerical Discretization

4.1.1 Incompressible Simulation

In the case of the first approach, a low dissipation methodology strategy [28] based on the recently proposed conservative EMAC scheme [29] is used with a Galerkin approximation for space discretization together with a non-incremental fractional step method to stabilise pressure. Temporal discretization will be performed through a conservative explicit third-order Runge-Kutta scheme [30].

4.1.2 Compressible Simulation

The NOISEtte code [31] has been used for the compressible simulation. It is based on the finite-volume EBR (Edge-Based Reconstruction) schemes [32] for unstructured hybrid meshes. This schemes provide a higher accuracy than most Godunov-type 2nd-order schemes at a low computing cost. On translationally-invariant (structured) mesh zones the EBR schemes coincide with high-order (up to 6th) finite-difference schemes. An implicit 2-nd order scheme with Newton linearization is used for the time integration.

4.2 Computational Grid

Computational grid design is a non trivial task and the characteristics of each CFD code needs to be taken into account before starting the process. For this reason, two type of meshes have been constructed for each type of simulation. The following subsections describe the specific features of each design. Nevertheless, the boundary conditions treatment have been similar for both cases.

4.2.1 Incompressible Simulation

A non-structured grid is used for the $x - y$ planes. The nodes are clustered near the walls, within the cavity and in the wake region (see Fig.5). After a mesh convergence study for which the pressure changed less than 0.5%, the resolution inside the whole cavity was decided to be 0.014 for the two-dimensional case (see Fig.6). The mesh for the 3D case has been created extruding the two-dimensional mesh. The number of parallel planes in the z direction is 100 with $\Delta z = 0.04$ (see Fig.7).

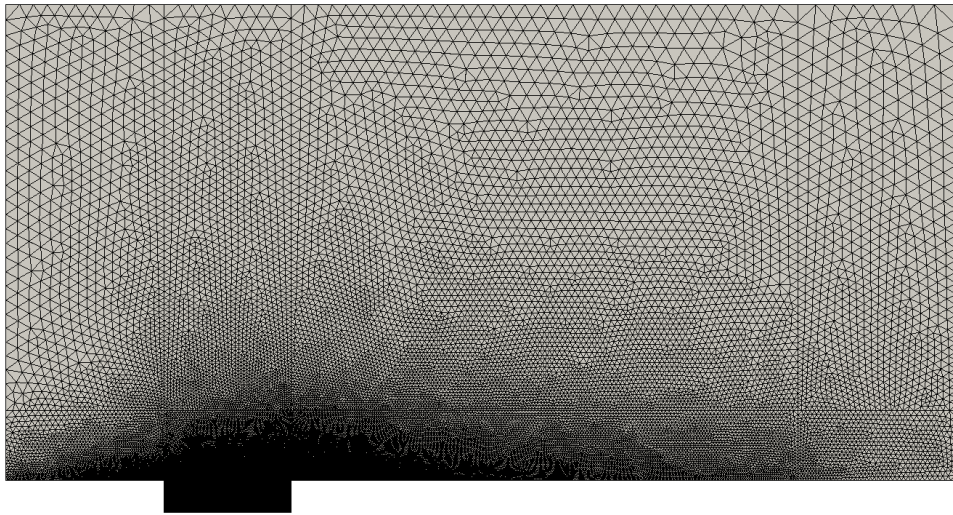


Figure 5: Grid in the $x - y$ plane for the incompressible case.

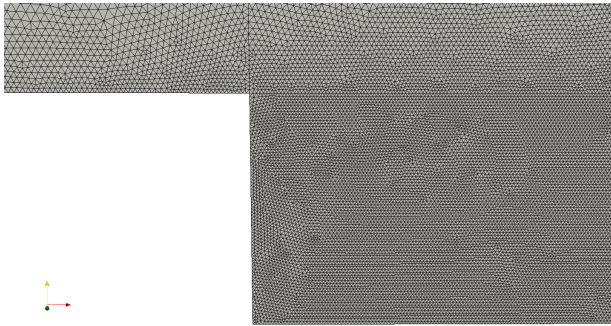


Figure 6: Grid in the $x - y$ plane at the cavity for the incompressible case.

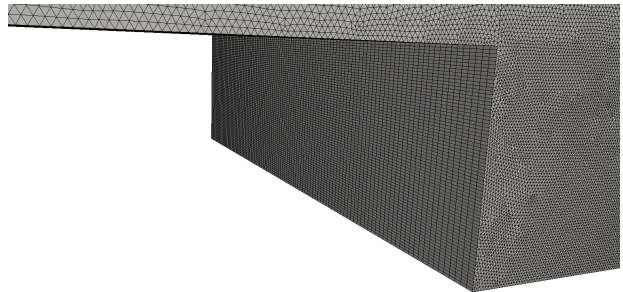


Figure 7: Grid in the streamwise direction at the cavity for the incompressible case.

4.2.2 Compressible Simulation

A structured and nonuniform grid is used for the $x - y$ planes. Similarly to the incompressible case, the nodes are clustered near the walls, within the cavity and in the wake region (see Fig.9). The resolution in the walls of the cavity is 0.004 and the total amount of elements is $8.7 \cdot 10^4$ (see Fig.8). The mesh for the 3D case has been also created extruding a two-dimensional mesh. The number of parallel planes in the z direction is 150 with $\Delta z = 0.027$.

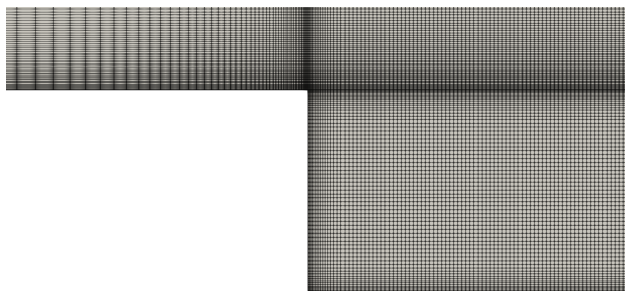


Figure 8: Grid in the $x-y$ plane at the cavity for the compressible case.

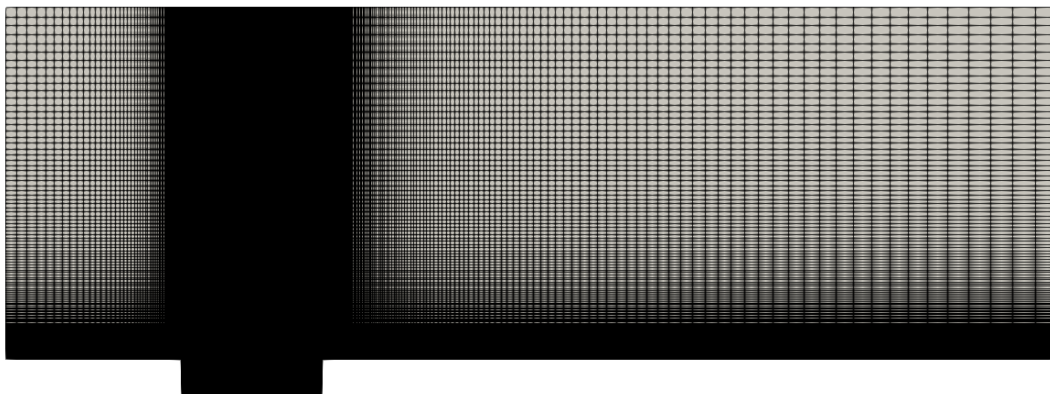


Figure 9: Grid in the $x-y$ plane for the compressible case.

4.3 Curle post-processing

The Curle approach in the form of Equation 12 has been implemented in a parallel code written in C language.

$$p(\mathbf{x}, t) - p_0 = \frac{1}{4\pi} \int_S -l_i n_j \left(\frac{1}{ra_0} [\dot{p}_{ij}] + \frac{1}{r^2} [p_{ij}] \right) dS \quad (12)$$

The pressure over the solid wall has to be stored for every time step, a process which occupies a high amount of disk space but is necessary for the calculation of Equation 12. In the case of the two-dimensional simulation, the pressure distribution has been assumed constant in z direction. Similarly, for the three-dimensional simulation the pressure has been stored for each plane of the computational domain and it has been assumed the same for all its shifted planes. The surface integral is extended along the spanwise direction until the contribution of a new plane is negligible. This convergence is assured due to the inverse dependence of expression 12 with distance.

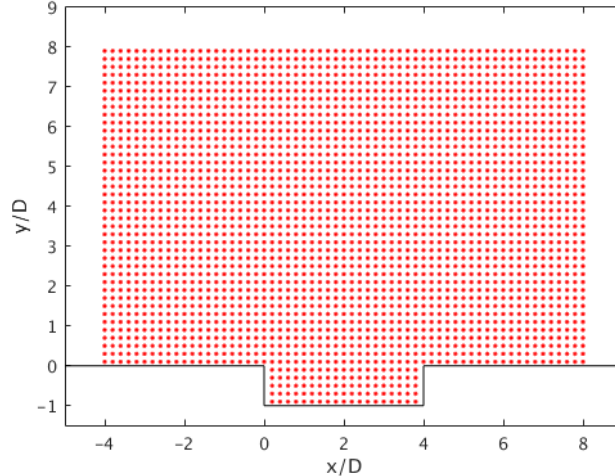


Figure 10: Acoustic domain.

Regarding the evaluation of each term of the integral in the retarded time $\tau = t - r/a_0$, a linear temporal interpolation has been used. The calculation of the integral is made every Δt for a total time range T . The specified sampling rate limits the maximum calculated frequency to $f_{max} = \frac{1}{\Delta t}$. On the other hand, to ensure that the lower frequency is properly sampled at least 10 complete periods should lie inside T , then the minimum frequency that can be captured is $f_{min} = \frac{10}{T}$.

Finally, a set of 2535 acoustic observers are distributed in a mesh around the cavity (see. Fig 10) located at plane $z = 0$. The acoustic pressure obtained from the Curle postprocess will be calculated for the location of these observers. An observer is located every $(\Delta x, \Delta y) = (0.2, 0.2)$.

5 Results

5.1 Flow Field Results

This section describes the results of computation of laminar flow past the two-dimensional and three-dimensional open cavity, the latter considering the flow first incompressible and then compressible. This work aims to first understand the effects of considering either two-dimensional or three-dimensional flow field results as acoustic sources and then to compare the compressibility effects in order to validate Curle's formulation. For this reason, both comparisons are made in separate sections. May the reader notice that to have statistically representative average variables for the three-dimensional simulations, these have been averaged not only in time but also in the spanwise direction.

5.1.1 Two-dimensional vs. Three-dimensional Incompressible Simulation

The streamlines of the instantaneous two-dimensional flow are illustrated in Fig.11. The flow is characterised by the creation of a vortex at the bottom left corner of the cavity. From there, it grows until the recirculation reaches the top left edge of the cavity and starts to pull down freestream fluid, creating a larger structure which in turn grows and moves downstream until the cavity trailing edge, where it is forced out by the vortex generated at the next period. Then, the vortical structures formed in the cavity edge travel almost unaltered downstream and attached to the wall of the domain.

The three dimensional flow behaves in a completely different manner, as can be seen in Figure 12 where the three-dimensional vortical structures identified by means of \mathcal{Q} -isocontours are represented. \mathcal{Q} [33] is the second invariant of the velocity gradient tensor defined as:

$$\mathcal{Q} = -\frac{1}{2} \frac{\partial u_i}{\partial x_j} \frac{\partial u_j}{\partial x_i} \quad (13)$$

Instabilities triggered by the interaction with the edge of the cavity start to develop and grow up, until at a certain distance from the cavity the flow transitions to turbulent, and a turbulent boundary layer develops downstream the cavity. The vortex stretching [34] is responsible for the enhancement of vorticity and the transport of energy towards the smaller scales. Thus, the three-dimensional deformation of the vortices formed close the edge of the cavity eventually leads to the break up into smaller vortices and vortical structures become more complicated downstream the cavity.

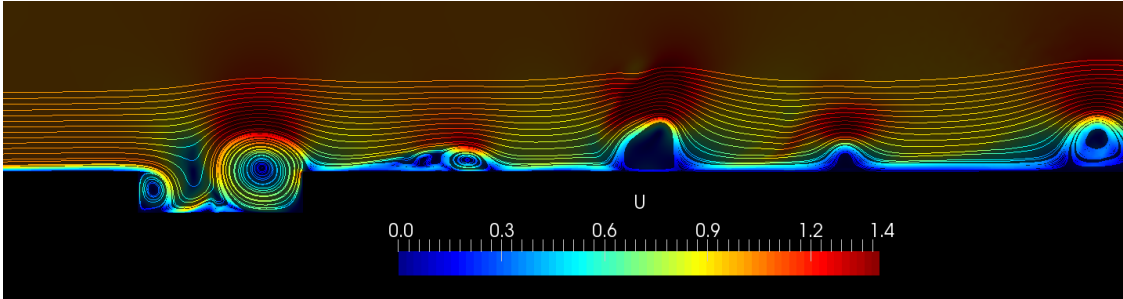


Figure 11: Streamlines for instantaneous velocity in the 2D case coloured by velocity magnitude.

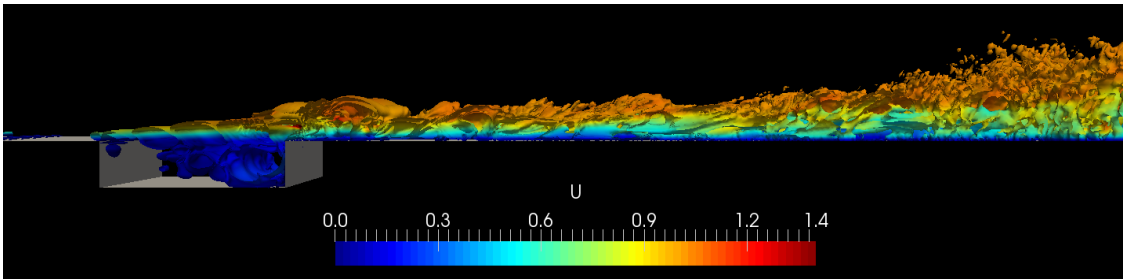


Figure 12: Q -isocontours in the three-dimensional case coloured by velocity magnitude.

The vortices appearing in the two-dimensional simulation do not vanish with time and as a consequence the pressure value over the wall changes completely. Figure 13 presents the time average $\langle p \rangle$ distribution along the wall, where s is the distance from the leading edge and the vertical lines define the corners of the cavity. The mean pressure is low on the upstream cavity wall and in the beginning of the cavity. For the two-dimensional case, then it rises steeply towards the end of the cavity and reaches a maximum in the bottom downstream corner followed by a minimum value at the trailing edge. On the contrary, the maximum value in the three-dimensional case occurs at the trailing edge of the cavity, due to the periodic impingement of the vortex detached from the shear layer. Overall, as will be seen in section 5.2, the higher absolute mean pressure over the whole wall for the two-dimensional case will result in a much higher acoustic pressure.

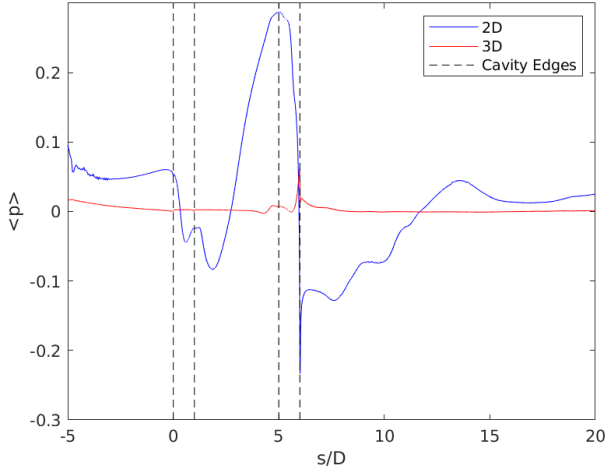


Figure 13: $\langle p \rangle$ profile along the wall.

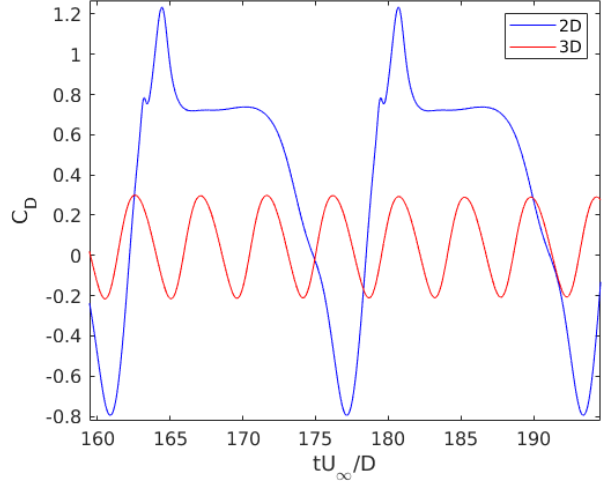


Figure 14: C_D time evolution for the 2D and 3D cases.

Further comparisons shows that cavity drag is also in high disagreement. The cavity drag is computed as

$$C_D = \frac{F_D}{\frac{1}{2}\rho_\infty U_\infty^2 D} \quad (14)$$

where F_D is the force contribution from the three cavity walls. Figure 14 shows the time evolution of C_D during two periods of the 2D case, for which the mean value is $\langle C_D \rangle = 0.407$, whereas for the three-dimensional case is $\langle C_D \rangle = 0.058$. The spectra of the oscillation is also substantially different. The fundamental frequencies, associated with the dimensionless frequency with the highest peak in the power spectrum, are $f_{2D} = 0.058$ and $f_{3D} = 0.220$.

J.E. Rossiter obtained an empirical equation predicting the oscillation frequencies of the cavity [35]:

$$f = \frac{U}{L} \frac{m - \gamma}{\left(\frac{1}{K} + M\right)} \quad (15)$$

where $m = 1, 2, 3, \dots$. The experimental values for γ and K derived for $L/D = 4$ were $\gamma = 0.25$ and $K = 0.57$. Using Eq.15, the predicted frequency stages for $M = 0.15$ using Rossiter's formula are displayed in table 1:

m	1	2	3
f	0.099	0.230	0.361

Table 1: Rossiter's frequencies for $L/D = 4$.

For such low Mach numbers, no empirical evidence of the stage $m = 1$ exists while the fundamental frequency f_{3D} is in good agreement with the second stage of oscillation predicted by Rossiter's formula. This result further emphasises the need of the use of a 3D simulation for acoustic field predictions even for low Reynolds numbers.

5.1.2 3D Incompressible vs. Compressible Simulation

It is the purpose of the present study to understand and explore the limits of use for the Curle's formulation. For this reason and taking advantage of the low Reynolds number, a comparison with the direct value for the acoustic pressure obtained from a compressible simulation without any sound modelling is performed. In order to evaluate the differences between the compressible and incompressible simulations, the flow variables

will be compared before considering acoustic pressures. Profiles of the mean velocity components, $\langle u \rangle$ and $\langle v \rangle$, along the y axis at the same streamwise positions are displayed in Figure 15 and 16.

Except for the difference at $x = 4D$ (trailing edge cavity), the results are in satisfactory agreement. Moreover, the cavity drag is also consistent with the results previously stated for the three-dimensional incompressible simulation. Table 2 shows the mean drag values and the fundamental frequencies obtained for all the cases studied.

Case	2D Incompressible	3D Incompressible	3D Compressible
$\langle C_D \rangle$	0.407	0.058	0.055
f	0.058	0.220	0.221

Table 2: Mean value of C_D and fundamental frequency.

The time average of the cavity drag is $\langle C_D \rangle = 0.055$ and the fundamental frequency is $f = 0.221$. However, the most critical point for later agreement in the acoustic field is the concordance of the mean pressure over the wall. The different compressibility treatment between both approaches generate a reference pressure offset, $p_{ref} = 31.7552$, between the calculated pressures. In order to make results comparable, such reference pressure has been subtracted from the compressible mean pressure. Figure 17 shows that the most discrepant part is the downstream wall of the cavity where the peaks of pressure are not correctly captured by the incompressible simulation. It is believed that this difference could be a consequence of the different grid resolution in this part of the cavity. Compressibility effects can also be a source of discrepancies between results even though the Mach number is considered low. However, the forthcoming acoustic results will show that these differences do not create significant differences in the frequency spectra.

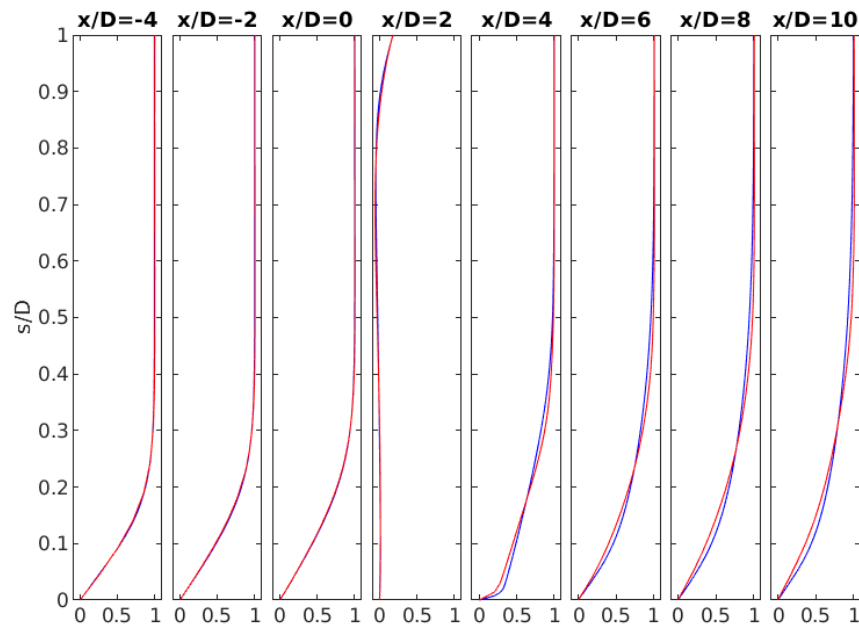


Figure 15: $\langle u \rangle$ profile comparison between the compressible and incompressible cases.

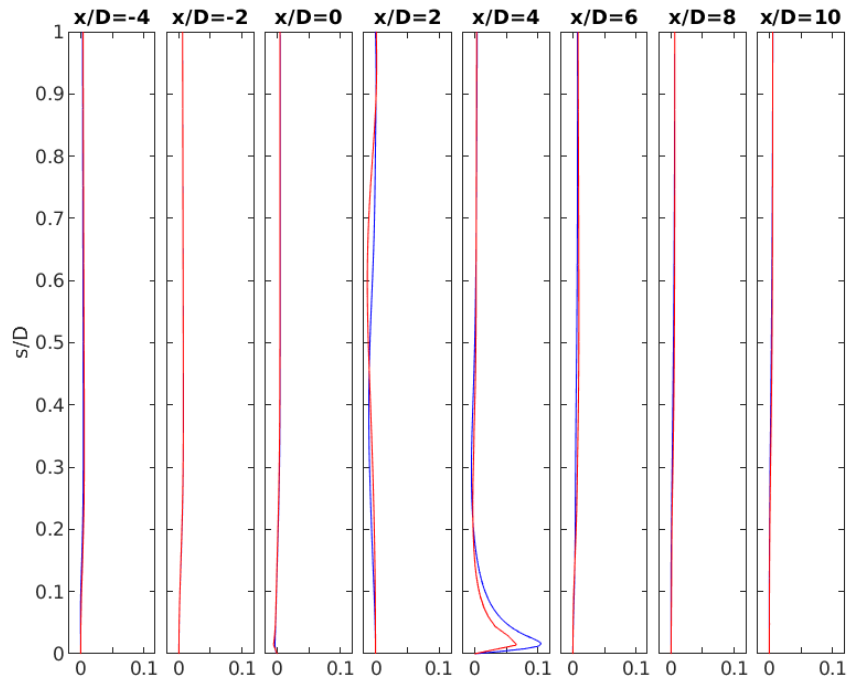


Figure 16: $\langle v \rangle$ profile comparison between the compressible and incompressible cases.

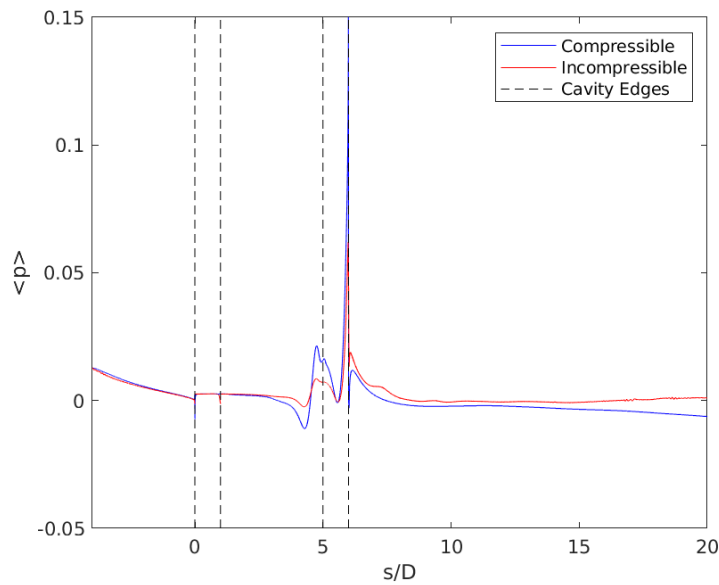


Figure 17: $\langle p \rangle$ profile along the walls.

5.2 Acoustic Results

5.2.1 Two-Dimensional vs. Three-Dimensional Incompressible Simulation

The average levels of $\langle p \rangle$ shown in Figure 13 decay to zero rapidly after the cavity trailing edge. This together with the inverse dependence with distance given by Eq.12 assures the convergence of the surface

integral for the observers located in Fig.10. For both cases, the surface of integration has been limited in the streamwise direction from $x = -4D$ to $x = 23D$ (avoiding the buffer zone) and in the spanwise direction from $z = -24D$ to $z = 24D$. The acoustic pressure signal has been calculated during 100 time units using a sampling rate of $\Delta t = 0.1 \frac{D}{U_\infty}$. This means that the lowest frequency that can be captured is $f_{min} = 0.1$ (to ensure that at least 10 cycles lie inside our sampling time range). Regarding the maximum frequency, two restrictions are accounted for: i) a numerical one, the sample rate, and ii) a physical one, the compactness of the cavity. The first limits the maximum frequency to $f_{max} = 10$, whereas the second to $f_{max} < \frac{a_0}{2\pi D} = \frac{U_\infty}{2M\pi D} = 1.06$. Therefore, the Curle formulation for the presented case is limited to the range of frequencies between $0.1 \leq f \leq 1$. As aforementioned, many studies have been devoted to this configuration assuming two-dimensional flow [14–16] and the present results are in fair agreement with them. However, as the pressure fluctuations in the wall do not vanish due the absence of vortex stretching, the acoustic results are very sensitive to the integration region used for the Curle integral, that should ideally reach infinite.

Figures 18 and 19 present the frequency spectra for the calculated acoustic signal for the observers located at $(x, y) = (0, 7.3)$ and $(x, y) = (2, 7.3)$. The Power Spectral Density (PSD) has been calculated using the Lomb-Scargle algorithm [36, 37]. As for the three-dimensional case there is one predominant frequency at $f = 0.220$, related with the shear layer vortex impingement, for the two-dimensional simulation most of the energy is contained in three frequencies, each a consecutive multiple of the vortex shedding frequency: $f_1 = 0.061$, $f_2 = 0.122$ and $f_3 = 0.184$.

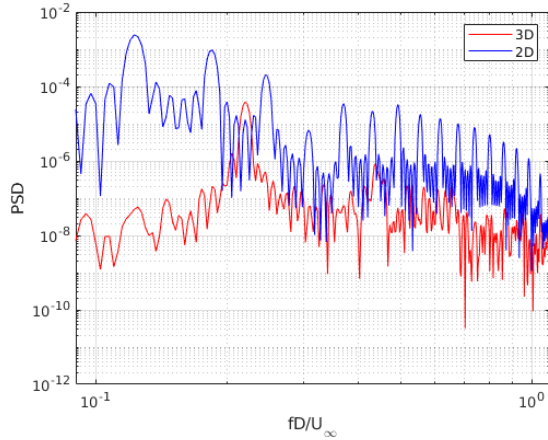


Figure 18: PSD at observer $(x, y) = (0, 7.3)$.

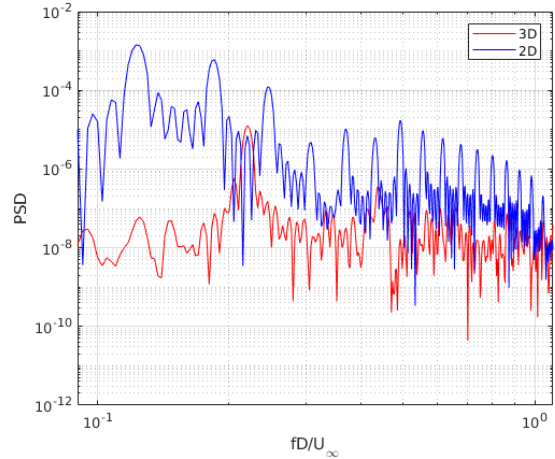


Figure 19: PSD at observer $(x, y) = (2, 7.3)$.

The pressure coefficient is defined as:

$$C_p = \frac{p - p_\infty}{\frac{1}{2}\rho_\infty U_\infty^2} \quad (16)$$

The value of C_p associated with the mean value of the acoustic pressure p'_{rms} is plotted in Figures 20 and 21. These maps show not only that the distribution of the acoustic pressure is much different but also that the overall value of p' over the whole map is approximately one order of magnitude higher for the two-dimensional case. Moreover, Figure 22 shows the directivity pattern for those observers located at distance 6 from the centre of the cavity located at $(x, y) = (2D, 0D)$. Although in both patterns the region with higher acoustic intensity is located between $\alpha_1 = 120^\circ$ and $\alpha_2 = 180^\circ$ (where α is the counterclockwise angle taken from the downstream wall), the two-dimensional calculation also predicts a high noise for those observers located behind the cavity. There is also a remarkable difference for the observers located between $\alpha_1 = 30^\circ$ and $\alpha_2 = 90^\circ$, a region to where the two-dimensional case hardly propagates sound whereas for the three-dimensional case there is not a significant minimum.

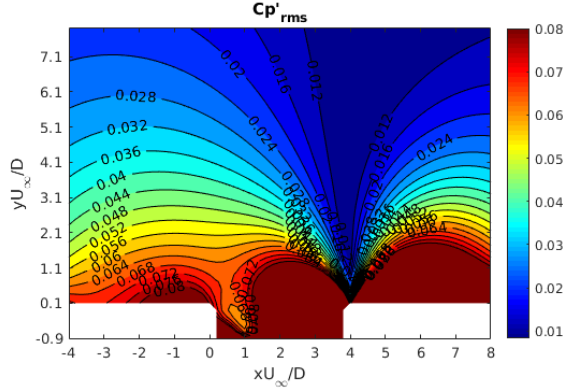


Figure 20: $C_{p'rms}$ map for the 2D case.

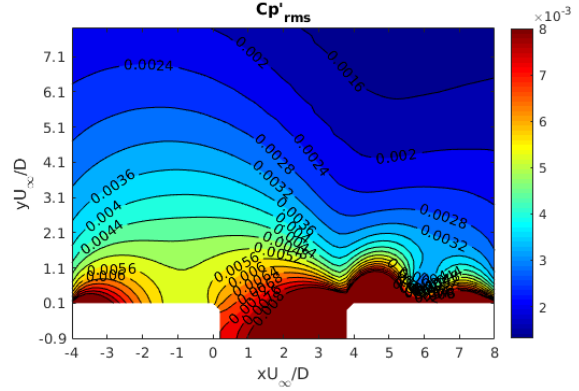


Figure 21: $C_{p'rms}$ map for the 3D case.

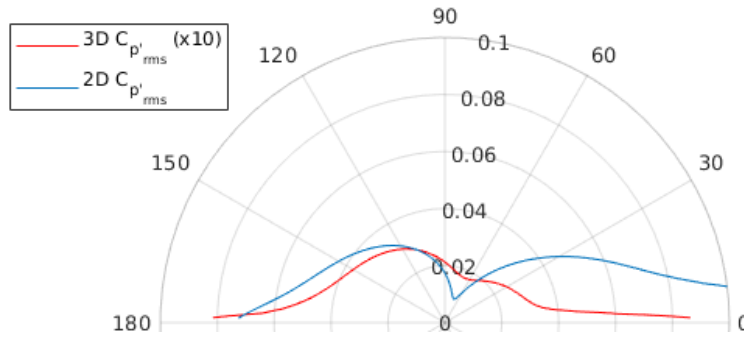


Figure 22: $C_{p'rms}$ directivity pattern.

5.2.2 Three-dimensional Incompressible vs. Compressible Simulation

Figures 23 and 24 display the frequency spectra for the calculated acoustic signal with Curle and with DS for the observers located at $(x, y) = (0, 7.3)$ and $(x, y) = (2, 7.3)$. Despite the overall energy of the signal calculated with Curle is lower, the frequencies are correctly correlated. Table 3 shows the two frequencies with higher PSD value for both cases:

Order	f_{Curle}	f_{DS}
1	0.220	0.437
2	0.219	0.438

Table 3: Two main frequencies and correspondent PSD values.

Given that the findings are based on a limited number of observers for the DS, the results from such analyses should be taken with care. Further analysis related with noise distribution and directivity will be made. Special attention should also be taken over the amplitude levels in further works.

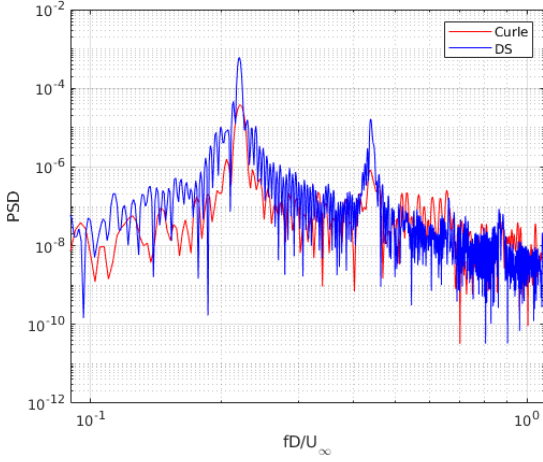


Figure 23: PSD at observer $(x, y) = (0, 7.3)$.

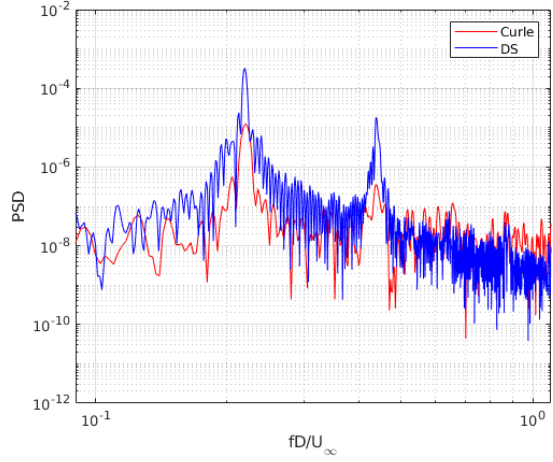


Figure 24: PSD at observer $(x, y) = (2, 7.3)$.

6 Conclusions

Numerical simulations of the sound radiated by a three-dimensional infinite open cavity at Reynolds number based on the cavity depth of $Re = 1500$ and Mach number of $M = 0.15$ have been performed, without any turbulence model. To do so, two approaches have been used: Curle integral, evaluated as a post-process of an incompressible solution and compressible direct simulation. For the incompressible approach, two-dimensional and three-dimensional simulations have been performed.

The results obtained after mesh convergence study show that two-dimensional and three-dimensional incompressible flow results are significantly different, as expected for a Reynolds number above the known transition value, at $Re \approx 1200$. The vortex stretching mechanism, responsible for the enhancement of vorticity and the transport of energy towards the smaller scales, is not present in the two-dimensional results and therefore the vortices do not vanish. As a consequence, the pressure value over the wall changes completely, as well as the drag and other flow parameters. The drag fundamental frequency in the three-dimensional results is in good agreement with published experimental data.

On the other hand, the three-dimensional compressible and incompressible flow results agree quite well, as expected for such a low Mach number. However, there are minor differences at the downstream wall of the cavity, both in velocity and pressure distributions, that could be due to mesh resolution.

Respect to the acoustic results, the two-dimensional incompressible simulations are in fair agreement with previous studies. However, the three-dimensional results are about an order of magnitude different. The $C_{p_{rms}}$ map, including acoustic directivity, is also in disagreement. Thus, a two-dimensional simulation would predict a high radiation to the downstream direction and a singular zone with hardly any noise propagation between $\alpha_1 = 60$ and $\alpha_2 = 90$. Such characterisation differs from the one obtained in the three-dimensional simulation, where the cavity radiates mainly towards upstream positions.

Respect to the comparison of the Curle formulation with a direct acoustic simulation, the present study has been limited to two observers far from the cavity. In these conditions, and in the range limited by compactness criteria and sampling time, the frequency spectra is in good agreement as expected.

Future work will be focused in: (i) The comparison of complete acoustic maps in order to precisely determine the regions where the Curle methodology yields accurate values. (ii) The use of pressure distributions obtained from compressible simulations to evaluate the Curle integral and clarify the role of the compressibility for this configuration at low Mach numbers.

7 Acknowledgements

This work was carried out within the framework of an Industrial Doctorate project from the government of Catalonia and was sponsored by the Agència de Gestió d'Ajuts Universitaris i de Recerca (AGAUR) and the automotive company SEAT S.A. The authors gratefully acknowledge the support provided by both organisms. The authors thankfully acknowledge the computer resources at MareNostrum and the technical support provided by Barcelona Supercomputing Center (FI-2016-3-0014).

References

- [1] Michael Hartmann, Joerg Ocker, Timo Lemke, Alexandra Mutzke, Volker Schwarz, Hironori Tokuno, Reinier Toppinga, Peter Unterlechner, and Gerhard Wickern. Wind noise caused by the side-mirror and a-pillar of a generic vehicle model. In *18th AIAA/CEAS Aeroacoustics Conference (33rd AIAA Aeroacoustics Conference)*, page 2205, 2012.
- [2] Franck Pérot, Xavier Gloerfelt, Christophe Bailly, Jean-Marc Auger, and H el ene Gardi. Numerical prediction of the noise radiated by a cylinder. In *9th AIAA/CEAS Aeroacoustics Conference and Exhibit*, page 3240, 2003.
- [3] Hua-Dong Yao, Lars Davidson, and Lars-Erik Eriksson. Noise radiated by low-reynolds number flows past a hemisphere at $ma= 0.3$. *Physics of Fluids*, 29(7):076102, 2017.
- [4] Claus Wagner, Thomas H uttl, and Pierre Sagaut. *Large-eddy simulation for acoustics*, volume 20. Cambridge University Press, 2007.
- [5] Christophe Bailly and Daniel Juve. Numerical solution of acoustic propagation problems using linearized euler equations. *AIAA journal*, 38(1):22–29, 2000.
- [6] Christophe Bailly and Christophe Bogey. An overview of numerical methods for acoustic wave propagation. 2006.
- [7] R Ewert and Wolfgang Schr oder. Acoustic perturbation equations based on flow decomposition via source filtering. *Journal of Computational Physics*, 188(2):365–398, 2003.
- [8] Michael J Lighthill. On sound generated aerodynamically. i. general theory. In *Proceedings of the Royal Society of London A: Mathematical, Physical and Engineering Sciences*, volume 211, pages 564–587. The Royal Society, 1952.
- [9] N Curle. The influence of solid boundaries upon aerodynamic sound. In *Proceedings of the Royal Society of London A: Mathematical, Physical and Engineering Sciences*, volume 231, pages 505–514. The Royal Society, 1955.
- [10] JE Ffowcs Williams and David L Hawkings. Sound generation by turbulence and surfaces in arbitrary motion. *Philosophical Transactions of the Royal Society of London A: Mathematical, Physical and Engineering Sciences*, 264(1151):321–342, 1969.
- [11] Jay C Hardin and D Stuart Pope. Sound generation by flow over a two-dimensional cavity. *AIAA journal*, 33(3):407–412, 1995.
- [12] Tim Colonius, Amit Basu, and Clarence Rowley. Numerical investigation of the flow past a cavity. In *5th AIAA/CEAS Aeroacoustics Conference and Exhibit*, page 1912, 1999.
- [13] X Gloerfelt, C Bailly, and D Juv e. Direct computation of the noise radiated by a subsonic cavity flow and application of integral methods. *Journal of Sound and Vibration*, 266(1):119–146, 2003.
- [14] Johan Larsson, Lars Davidson, Magnus Olsson, and Lars-Erik Eriksson. Aeroacoustic investigation of an open cavity at low mach number. *AIAA journal*, 42(12):2462–2473, 2004.
- [15] Jonas Ask and Lars Davidson. An acoustic analogy applied to the laminar upstream flow over an open 2d cavity. *Comptes Rendus Mecanique*, 333(9):660–665, 2005.
- [16] Jonas Ask and Lars Davidson. Sound generation and radiation of an open two-dimensional cavity. *AIAA J*, 47(6):1337–1349, 2009.
- [17] Guillaume A Bres and Tim Colonius. Three-dimensional instabilities in compressible flow over open cavities. *Journal of Fluid Mechanics*, 599:309–339, 2008.
- [18] Thierry M Faure, Panayotis Adrianos, Fran ois Lusseyran, and Luc Pastur. Visualizations of the flow inside an open cavity at medium range reynolds numbers. *Experiments in Fluids*, 42(2):169–184, 2007.
- [19] Huanxin Lai and Kai H Luo. A three-dimensional hybrid les-acoustic analogy method for predicting open-cavity noise. *Flow, turbulence and Combustion*, 79(1):55–82, 2007.

- [20] Hua-Dong Yao, Lars Davidson, Lars-Erik Eriksson, Shia-Hui Peng, Olof Grundestam, and Peter E Eliasson. Surface integral analogy approaches for predicting noise from 3d high-lift low-noise wings. *Acta Mechanica Sinica*, 30(3):326–338, 2014.
- [21] Johan Larsson, Lars Davidson, Magnus Olsson, and Lars-Erik Eriksson. Aeroacoustic investigation of an open cavity at low mach number. *AIAA journal*, 42(12):2462–2473, 2004.
- [22] F Farassat and MK Myers. Extension of kirchhoff’s formula to radiation from moving surfaces. *Journal of Sound and Vibration*, 123(3):451–460, 1988.
- [23] Gustav Kirchhoff. Zur theorie der lichtstrahlen. *Annalen der Physik*, 254(4):663–695, 1883.
- [24] Ulf Michel. History of acoustic beamforming. In *1st. Berlin Beamforming Conference*, 2006.
- [25] Sjoerd W Rienstra and Avraham Hirschberg. An introduction to acoustics.
- [26] M Gharib and A Roshko. The effect of flow oscillations on cavity drag. *Journal of Fluid Mechanics*, 177:501–530, 1987.
- [27] Mariano Vázquez, Guillaume Houzeaux, Seid Koric, Antoni Artigues, Jazmin Aguado-Sierra, Ruth Arís, Daniel Mira, Hadrien Calmet, Fernando Cucchietti, Herbert Owen, et al. Alya: Multiphysics engineering simulation toward exascale. *Journal of Computational Science*, 14:15–27, 2016.
- [28] O Lehmkuhl, G Houzeaux, M Avila, H Owen, M Vazquez, and D Mira. A low dissipation finite element scheme for the large eddy simulation on complex geometries. In *19h International Conference on Finite Elements in Flow Problems-FEF*, 2017.
- [29] Sergey Charnyi, Timo Heister, Maxim A Olshanskii, and Leo G Rebholz. On conservation laws of navier–stokes galerkin discretizations. *Journal of Computational Physics*, 337:289–308, 2017.
- [30] Francesco Capuano, Gennaro Coppola, Luis Rández, and Luigi de Luca. Explicit runge–kutta schemes for incompressible flow with improved energy-conservation properties. *Journal of Computational Physics*, 328:86–94, 2017.
- [31] A Gorobets. Parallel algorithm of the noisette code for cfd and caa simulations. *Lobachevskii Journal of Mathematics*, 39(4):524–532, 2018.
- [32] Pavel Bakhvalov and Tatiana Kozubskaya. Ebr-weno scheme for solving gas dynamics problems with discontinuities on unstructured meshes. *Computers & Fluids*, 157:312–324, 2017.
- [33] Jinhee Jeong and Fazle Hussain. On the identification of a vortex. *Journal of fluid mechanics*, 285:69–94, 1995.
- [34] Hendrik Tennekes and John Leask Lumley. *A first course in turbulence*. MIT press, 1972.
- [35] JE Rossiter. Wind tunnel experiments on the flow over rectangular cavities at subsonic and transonic speeds. Technical report, Ministry of Aviation; Royal Aircraft Establishment; RAE Farnborough, 1964.
- [36] Nicholas R Lomb. Least-squares frequency analysis of unequally spaced data. *Astrophysics and space science*, 39(2):447–462, 1976.
- [37] Jeffrey D Scargle. Studies in astronomical time series analysis. ii-statistical aspects of spectral analysis of unevenly spaced data. *The Astrophysical Journal*, 263:835–853, 1982.